# METHODS AND PROCEDURES FOR RE-ENTRY PREDICTIONS AT ESA

**H. Klinkrad**

*Space Debris Office, ESA/ESOC, Darmstadt, Germany, Email: Heiner.Klinkrad@esa.int*

## ABSTRACT

Since more than 30 years ESA has been performing re-entry predictions for potentially hazardous space objects that may pose a risk either due to large casualty cross-sections of parts surviving to ground impact, or due to hazardous substances that could be released into the atmosphere or on the Earth surface. Some of the more prominent objects that belonged to this category were Cosmos-954, Skylab, Cosmos-1402 and Salyut-7. To predict the re-entry time windows of such objects and the related ground swaths at risk ESA uses a comprehensive suite of software tools that cover all major facets of this complex, multi-disciplinary problem. In the following paper software implementations of mathematical algorithms will be outlined that describe physical phenomena of re-entry events and yield a spectrum of resulting data products.

Key words: re-entry prediction; re-entry break-up; orbit theories; atmosphere models.

## 1. INTRODUCTION

About 7,000 tonnes of man-made, Earth orbiting objects are concentrated to more than 99% in the routinely tracked catalog objects of the US Space Surveillance Network (SSN). Some 40% thereof reside in or pass through the low Earth orbit regime (LEO). On the average, approximately 100 tonnes of this mass annually re-enter into the Earth atmosphere in an uncontrolled manner. This corresponds to $\sim$2 catalog objects per day, and $\sim$2 catalog objects larger than $1\mathrm{m}^2$ each week. As space objects reach masses above a few 100 kg, the likelyhood of fragments reaching ground increases, and the risk to the population increases accordingly. For orbital masses beyond 1 tonne there is a high probability that their risk to the ground population exceeds a widely accepted threshold of 1 in 10,000 for a single event. Such objects require special attention in terms of re-entry monitoring and prediction of the entry time window, its associated ground swath, and the resulting ground risk in terms of land impact probability and casualty probability.

ESA's Space Debris Office and its staff look back to a long history of re-entry predictions, with a well developed expertise that reaches back to the 1970s, when the 78 ton Skylab space station was abandonned in February 1974, and re-entered over the Indian Ocean and Australia on July 11, 1979, during the peak of solar cycle 21 [5]. Less than 4 years later, in early 1983, the dysfunctional, reactor-equipped Cosmos-1402 satellite decayed in two parts. Its detached radar payload re-entered over the India Ocean on January 23, and its reactor/propulsion unit re-entered over the South Atlantic Ocean, near the Brazilian coastline, on February 7 [1]. This was the first occasion at which ESA communicated prediction results to national authorities of its Member States.

On February 7, 1991, almost 9 years after its on-orbit deployment, the Salyut-7 space station with the attached Cosmos-1686 module re-entered over Chile and Argentina. After it was mothballed in November 1985 the 40 ton compound started its orbit decay, with limited propellant reserves and maneuvering capabilities that finally led to an overshoot of the South Pacific re-entry target area [2], with an impact footprint that extended across the South American continent.

In 1993 the Inter-Agency Space Debris Coordination Committee (IADC) was formed by its founding members NASA (USA), RSA (Russia), NASDA (Japan) and ESA (Europe), with the aim to foster the exchange of information on space debris measurements, modeling, mitigation and protection. Today, IADC has 12 member agencies that represent all major space faring nations. In 1997 IADC decided to install an information exchange system that facilitates the assessment of uncontrolled re-entry events through the assured availability and sharing of orbit determinations and re-entry predictions. The web-based IADC Re-Entry Events Database (REDB) was installed at ESA's Space Operations Centre (ESOC) in 1998 and has been in use since. Its functionality and the availability of re-entry prediction systems by IADC members is verified in at least one test campaign per year, with 15 such campaigns conducted through 2012.

ESA has developed a well-proven set of methods and tools to perform long-, medium- and short-term predictions of uncontrolled re-entry events. The underlying physical and mathematical models, achievable prediction accuracies, and typical output results will be summarized in this paper for a few representatives IADC re-entry campaigns.

*Proc. '6th European Conference on Space Debris'*
*Darmstadt, Germany, 22–25 April 2013 (ESA SP-723, August 2013)*

## 2. ORBIT STATE FORMATS AND PROPAGATION METHODS

The most comprehensive orbit state information on Earth orbiting objects is contained in the USSPACECOM space surveillance catalog. This catalog is maintained with radar and optical tracking data that are provided by a world-wide sensor system of the US Space Surveillance Network (SSN). Its observation data are used to establish and maintain orbit information on $\sim$23,000 objects larger than 10 cm in LEO and larger that 1 m in GEO. Some 17,000 of these data sets are available to registered users of the "space-track" data exchange platform that is operated by USSPACECOM's Joint Space Operations Center (JSpOC). These orbit data are provided in the format of Two-Line Element sets (TLE) as doubly averaged Kepler-type data where short- and long-term perturbations of dominant zonals harmonics are removed according to Brouwer's orbit theory. The SGP-4/SDP-4 orbit propagation software can be used to propagate TLE data sets, and to derive 1st order (accurate to $J_2$ only) osculating cartesian state vectors at the target epoch.

Depending on the propagation time span ESA uses two different orbit prediction techniques: a semi-analytical propagator for long- and medium-term predictions, and a numerical propagator for short-term predictions.

### 2.1. Semi-Analytical Long- and Medium-Term Propagation

ESA's semi-analytical approach uses singly-averaged Kepler-type elements. These elements are derived through Liu's theory from osculating cartesian states that are generated from TLE data through the SGP-4 theory [4]. Let an osculating Kepler state be defined as $\psi_j = a, e, i, \Omega, \omega, M$ $(j = 1, \ldots, 6)$, with its corresponding time rates of change $d\psi_j/dt = \dot{a}, \dot{e}, \dot{i}, \dot{\Omega}, \dot{\omega}, \dot{M}$, then the averaged time rates of change are defined as

$$\frac{\bar{\psi}_j}{dt} = \frac{1}{2\pi}\int_0^{2\pi} \frac{d\psi_j}{dt}\, dM \tag{1}$$

Through this operation, the high-frequency short-periodic perturbation spectrum is removed, and the remaining, much smoother long-periodic signal allows a significant increase in propagation time steps, which can be more than two orders of magnitude larger than those of numerical propagators using osculating states.

Eq. 1 can be analytically integrated for geopotential perturbations and 3rd body perturbations. For this purpose ESA uses expansions in eccentricity functions and inclination functions according to Kaula, Giacaglia and Cook, considering a truncated geopotential up to degree 8, and considering point masses for Sun and Moon, with positions determined by analytical ephemerides. Solar radiation pressure perturbations are integrated in a closed-form manner using Aksnes' theory for an oblate, cylindrical core shadow. Airdrag, being the only non-conservative perturbation, deserves special attention. The related modelling effort leads to complex perturbation equations that are not suited for analytical averaging. The drag effect on the time rate of change of the osculating semimajor axis, for instance, can be approximated by

$$\frac{d\psi_1}{dt} = \frac{da}{dt} = -c_D \frac{A}{m}\rho\, v\, a\, \frac{1 + e^2 + 2e\cos f}{1 - e^2} \tag{2}$$

where $c_D$ is the drag coefficient that is a function of the flow regime, $A/m$ is the area-to-mass ratio that can change with the attitude, $\rho$ is the air density that is a complex function of ambient conditions, and $v$ is the aerodynamic velocity that is affected by atmospheric co-rotation and winds. In order to apply Eq. 1 to Eq. 2 (and to the remaining drag equations), a Gauss quadrature scheme is employed.

$$\frac{\bar{\psi}_j}{dt} \approx \frac{1}{2}\sum_{n=1}^{N} w_n \cdot \frac{d\psi_j}{dt}\,(M_n) \tag{3}$$

Here, $M_n = \pi(1 + x_n)$ are distinct positions over one orbit, with assigned weights $w_n = 2 \cdot (P_N^{'}(x_n))^2/(1 - x_n^2)$, where $x_n \in [-1, +1]$ is the $n^{\text{th}}$ zero-transition of the Legendre polynomial $P_N(x)$ of order $N = 21$, with its derivative $P_N^{'}(x) = d(P_N(x))/dx$.

Based on the principle of "separation of perturbations", individual singly-averaged contributions from each perturbation effect are overlaid to determine the overall time rates of change for each of the 6 orbital elements at a given epoch. The corresponding time evolution of the orbital elements is determined by a numerical integration of the averaged equations of motion, using a $4^{\text{th}}$ order Adams-Bashforth/Adams-Moulton predictor/corrector method with step sizes of a few orbits for long-term forecasts down to fractions of an orbit near the altitude of $\sim$ 200 km, where a hand-over to a purely numerical integration is performed.

### 2.2. Numerical Short-Term Propagation

For the final phase of a re-entry, typically below 200 km altitude, some of the assumptions used in analytical or semi-analytical approaches tend to become invalid. Examples are (1) the assumption that the orbit can be regarded as invariant during a closed-form integration or quadrature of the perturbation equations, and (2) the assumption that $J_2$ is the only first order perturbation term. Besides, below 200 km the free-molecular flow regime changes to a hypersonic continuum regime, with an intermediate transition flow. All these considerations necessarily lead to a classical numerical integation of the perturbed equations of motion. To avoid singularities and allow a smooth transition from orbital motion to atmospheric free fall, this integration is performed in terms of osculating cartesian state vectors by means of a robust, step-size controlled Runge-Kutta $4^{\text{th}}$ order integrator. The applied perturbation model (geopotential, 3rd body, airdrag and radiation pressure) is carried over from the semi-analytical integration with adjustments and extensions, particulary for the airdrag model. The integration step size for the numerical propagation decreases from a few minutes at the 200 km interface to fractions of a minute during the atmospheric free fall.

The numerical integration uses osculating orbital elements. They are derived from a singly-averaged orbit state that is handed over at end of the semi-analytical propagation arc at about 200 km. The state transformation is explicit and to first order ($J_2$) accuracy only, according to Liu's orbit theory.

## 3. CONSTITUENTS OF THE AIRDRAG MODEL

The orbit energy loss is solely governed by the airdrag effect on the semimajor axis of the orbit, as described by Eq. 2. For the dominant class of near-circular re-entry orbits, this equation can be further simplified to

$$\frac{da}{dt} = -c_D \frac{A}{m} \rho \, v \, a \tag{4}$$

In this equation the parameters that are critical for a reliable re-entry forecast are (1) the drag coefficient $c_D$, (2) the area-to-mass ratio $A/m$, (3) the air density $\rho$, and (4) the aerodynamic velocity $v$. Related model assumptions shall now be explained in more detail.

### 3.1. Air Drag Coefficient

In aerodynamic terms the drag coefficient is a proportionality factor that describes the interaction of the ambient atmosphere with an object of given shape, cross-section, surface properties and aerodynamic velocity. The related acceleration $\vec{p}_D$ acts opposite to the aerodynamic velocity vector $\vec{v}$, proportional to $v^2$, and proportional to the area-to-mass ratio $A/m$, with a scaling drag paramenter $c_D$ as proportionality factor.

$$\vec{p}_D = -c_D \frac{A}{m} \, v \, \vec{v} \tag{5}$$

The different flow regimes of a space object as it re-enters into the Earth atmosphere can be coarsely described by its Knudsen number $\mathrm{Kn} = \lambda_{\mathrm{mol}}/\mathrm{L}_{\mathrm{ref}}$, where $\lambda_{\mathrm{mol}}$ is the mean free path length of air molecules and $L_{\mathrm{ref}}$ is a characteristic length of the entry object. Three major regimes can be distinguished.

- free molecular regime: $\mathrm{Kn} > 10$
  with $c_D = \mathrm{fct}(\mathrm{angles}, \mathrm{S}, \mathrm{T_w/T})$
- transitional regime: $0.01 \leq \mathrm{Kn} \leq 10$
  with $c_D = \mathrm{fct}(\mathrm{angles}, \mathrm{shape}, \mathrm{Kn}, \mathrm{T_w/T})$
- continuum regime: $\mathrm{Kn} < 0.01$
  with $c_D = \mathrm{fct}(\mathrm{angles}, \mathrm{shape}, \mathrm{Ma})$

where $\mathrm{S} = \mathrm{v}/\bar{\mathrm{v}}_{\mathrm{mol}} = \mathrm{v}/\sqrt{2\mathrm{RT}/\bar{\mathrm{M}}}$ is the molecular speed ration (aerodynamic velocity related to the mean Maxwellian velocity of air molecules) and $\mathrm{Ma} = \mathrm{v}/\bar{\mathrm{c}} = \mathrm{v}/\sqrt{\kappa\mathrm{RT}/\bar{\mathrm{M}}}$ is the Mach number (aerodynamic velocity related to the speed of sound in the ambient atmosphere). Due to the dependency of Knudsen and Mach numbers on $\sqrt{T/\bar{M}}$, also the drag coefficient may experience noticible variations with temperature and mean molecular mass. As a consequence, for instance, $c_D$ can increase by almost a factor of 2 in a Helium dominated environment, at 800 km for low solar activities. For the final re-entry phase the variation of the drag coefficient is accounted for in ESA's predictions by analytical expressions, as a function of the flow regime and of the basic shape of the entry object, as described in [2] and [5].

### 3.2. Area-to-Mass Ratio

When concentrating on uncontrolled re-entries one may assume that the entry object (mostly a spacecraft or orbital stage) has a known mass, and no means of active attitude control. Hence, the object is mostly undergoing a complex attitude motion under the joint influence of aerodynamic and gravity gradient torques. For the Russian Mir station, during its passive phase, two concurrent, orthogonal rotations were observed at periods of 6 min and 15 min respectively. The aerodynamic cross-section of Mir varied between 170 $\mathrm{m}^2$ and 470 $\mathrm{m}^2$, with a mean value of 385 $\mathrm{m}^2$. For a mass of 135 tonnes the mean cross-section led to a calibrated drag coefficient of $c_D = 2.214 \pm 0.043$ during the last month of natural orbit decay, with harmonic variations of increasing frequency with reducing orbit lifetime.

In the case of Skylab, the effective cross-section was used as a means to control the final entry location. Using some remnant attitude control capability, Skylab was turned from a torque-equilibrium attitude into an end-over-end tumbling mode, thus extending the orbit lifetime by about 20% and shifting the impact swath by approximately 1/2 revolution. This strategy also led to a casualty risk reduction by more than 20%.

### 3.3. Air Density

For orbit lifetime predictions and re-entry assessments a multitude of atmospheric models is available. ESOC uses a hybrid model consisting of MSIS90e and CIRA72 (see [4]). MSIS90e is based on in-situ mass spectrometer and ground-based incoherent scatter measurements to determine individual concentrations of the atmospheric species $\mathrm{N}_2$, N, $\mathrm{O}_2$, O, He, H and Ar, total densities $\rho$, local temperatures $T$, and exospheric temperatures $T_\infty$. This model uses analytical, species-wise concentration profiles, and likewise analytical temperature models as a function of altitude, applying low degree and order harmonic expansions to fit profile parameters as a function of longitude, latitude, local solar time, universal time, day of the year, actual and mean solar activity, and geomagnetic activity. As far as number densities of constituents and total air densities are concerned, MSIS90e is largely relying on satellite-based measurements, which are hence constrained to orbital altitudes above $\sim$ 200 km. In contrast to MSIS90e, CIRA72 is mainly based on drag observations of satellite orbits and uses numerically integrated diffusion equations for a reduced set of constituents. All dependencies on atmospheric paramenters are mapped onto the exospheric temperature $T_\infty$ that drives the concentration profiles and the total density.

Since the majority of MSIS90e and CIRA72 measurement data were collected at different, complementary altitudes, the reliability of the models is expected to be related to these sampling statistics. Hence, ESA uses a hybrid atmosphere model, with MSIS90e applied down to 200 km and again below 90 km, with CIRA72 being used between 200 km and 90 km, with altitude dependent weighting functions to allow smooth transitions. Quantities that determine the flow regime, such as $\mathrm{Kn}$ and $\mathrm{Ma}$ numbers, are computed along with the drag-relevant total density $\rho$ at each prediction step. For the semi-analytical propagation of the singly-averaged orbit state at each prediction time step a transformation to osculating elements is performed to account for short-periodic changes of the orbit radius, and hence of the geodetic altitude with amplitutes up to $\Delta H = \pm 2$ km.

### 3.4. Aerodynamic Velocity

Both, the semi-analytical long-term and the numerical short-term re-entry prediction methods are able to accept detailed models of the aerodynamic velocity. In both processes they are implemented in terms of osculating elements, and they allow to consider atmospheric corotation and effects from horizontal winds. Most re-entry objects, after passing through the Knudsen and Mach flow regimes, will enter into a state of equilibrium free-fall, governed by the Reynolds number $\mathrm{Re} = \mathrm{L_{ref}v}/\eta$, where $L_{\mathrm{ref}}$ is a characteristic length of the object, and $\eta$ is the dynamic viscosity of the ambient atmosphere. The free-fall ground impact velocity can be approximated as

$$v_{\mathrm{imp}} \approx \sqrt{\frac{2mg_\circ}{c_D A \rho_\circ}} \tag{6}$$

where $g_\circ$ is gravity acceleration and $\rho_\circ$ is the air density at ground level.

### 3.5. Solar and Geomagnetic Activity

Atmospheric models strongly depend on the interaction of the Earth's thermosphere with solar radiation and solar winds. ESA has devised methods to take account for both of these effects in re-entry predictions.

Solar radiation mainly heats the thermosphere through the absorption of EUV radiation that is emitted from Sun spots, particularly at peaks of the 11 year solar cycle. This EUV radiation is strongly correlated with the emmission of radio signals at the 10.7 cm wavelength which can be observed from ground, and which are measured in solar flux units, where $1\mathrm{SFU} = 10^{-22}\mathrm{W}/(\mathrm{m}^2\mathrm{Hz})$. This 10.7 cm solar flux ($F_{10.7}$) is correlated with a Sun spot index ($R$). Their combined data record reaches back into the 17th century, and it is used by ESA to perform long-term activity forecasts (one or more solar cycles) through a McNish/Lincoln technique, where a mean solar cylce is established from historic data, and modulations for predicted cycles are forecast from offsets of recent data from the mean cycle. Short-term forecasts (for 1 solar rotation of 27 days) are performed with an ARIMA process (auto-regressive integrated moving average) based on flux data of the past 24 months.

Solar winds, mainly in the form of $\mathrm{H}^+$ and $\mathrm{He}^{++}$ ions, interacts with the Earth's magnetic field and causes thermospheric heating due to the motion of these charged particles (Coulomb effect). Short-term geomagnetic activity effects, associated with the 27 day solar rotation period, can be predicted with some certainty. For long-term effects, however, only the higher frequency of solar wind occurences with peaks in the flux cycle can be correlated and accounted for as a low-amplitude signal of the $A_p$ or $k_p$ planetary geomagnetic index.

### 3.6. Calibration of the Ballistic Paramenter

In Eq.4 the term $B = c_D \cdot A/m$ is denoted as the *ballistic parameter* of an object in the orbital or re-entry phase. For practical applications in re-entry forecasts of an uncontrolled object one may assume that its mass remains constant down to a possible break-up altitude which is typically near 80 km. Over sufficiently short fitting arcs, compatible with the rotation rate of the object, one may also assume that the aerodynamic cross-section can be approximated by a mean value. The only variable quantity of the ballistic parameter $B$, and in the proportional decay rate $\dot{a}$ of the semimajor axis according to Eq.1 would then be the drag coefficient $c_D$ that can be directly fitted to an observed decay history $\dot{\bar{a}}(t)$ of the singly-averaged semimajor axis, where $\bar{a}(t)$ is determined from a TLE history of $\bar{a}(t)$. The time spans of the fitting arcs differ in length from $\sim$ 1 month in the early decay phase, to $\sim$ 1 week at until a few days before the re-entry, to $\sim$ 1 day in the final phase. These decreasing fitting spans reflect the increase in attitude dynamics with increasing air density. ESA uses three different ways of scaling $c_D$:

- single-step calibration by fitting a low order polynomial to $\bar{a}(t)$ and by analytically determining its time derivative $\dot{\bar{a}}(t_\circ)$ at the epoch of the last available state;
- backward shooting from $t_\circ$ to the start epoch of the fitting arc at $t_{-\mathrm{n}}$ until $\bar{a}(t_{-\mathrm{n}})$ is matched with sufficient accuracy; and

- a least squares backward fit over all $n$ data points $\bar{a}(t)$ for $t \in [t_\circ, t_{-\mathrm{n}}]$.

These methods can also be used in succession to guarantee and accelerate the convergence of the process. The rms error of fitting $\bar{a}(t)$ through a $c_D$ calibration can be less than 10 m in the early decay phase, and it can exceed 100 m close to the final re-entry. The uncertainty in the $c_D$ value itself is typically within $\pm 10\%$ until the final day of the orbit lifetime.

### 3.7. Re-Entry Casualty Risk Assessment

A spacecraft or rocket orbital stage that re-enters naturally, in an uncontrolled fashion, typically follows a fixed pattern. Let $t_\circ$ be the epoch when the intact object would reach the ground level, then at $t_\circ - 45$ min ($\sim 120$ km) it would start its final descent and enter into the regime of atmospheric flight. At about $t_\circ - 10$ min ($\sim 95 \pm 5$ km) large appendices would be torn off, followed by a phase of peak heating at $t_\circ - 6$ min ($\sim$ $60 \pm 10$ km) and maximum deceleration at $t_\circ - 4$ min ($\sim$ $45 \pm 10$ km). The combined aerothermal and aerodynamic loads normally lead to a break-up near $\sim$ $78 \pm 5$ km at approximately $t_\circ - 8$ min. Those break-up fragments that do not demise can cause a casualty risk to the population in the endangered ground swath. The object-specific risk can be expressed in terms of a casualty cross-section. If $A_\mathrm{h} = 0.36\,\mathrm{m}^2$ is adopted as a projected mean human cross-section, then the total casualty cross-section $A_\mathrm{c}$ of an entry event is defined by the following summation over all $K$ fragments that reach the ground.

$$A_\mathrm{c} = \sum_{k=1}^{K} \left( \sqrt{A_\mathrm{h}} + \sqrt{A_\mathrm{k}} \right)^2 \tag{7}$$

For practical applications in operational re-entry predictions one can assume that $A_\mathrm{c}$ is distributed across a ground swath that follows a 2-dimensional Gaussian impact probability density distribution function $p_\mathrm{i}(\lambda, \phi)$, with its major axis aligned with the ground track. Each swath position in terms of longitude $\lambda$ and latitude $\phi$ can also be associated with a corresponding population density $\rho(\lambda, \phi)$. If $x$ and $y$ are the swath coordinates in along-track and cross-track direction, centered on the most probable impact location, and if $x_{2\sigma}$ and $y_{2\sigma}$ are the $2\sigma$ extensions of the ground swath impact distribution, then the casualty probability is defined as

$$P_{\mathrm{c},2\sigma} = A_\mathrm{c} \int_{-x_{2\sigma}}^{+x_{2\sigma}} \int_{-y_{2\sigma}}^{+y_{2\sigma}} p_\mathrm{i}(x,y) \cdot \rho(x,y) \;\, \mathrm{d}y\, \mathrm{d}x \tag{8}$$

The 2D Gaussian impact probability density distribution $p_\mathrm{i}(x,y)$ and the population density $\rho(x,y)$ in Eq.8 can then be discretized with a resolution $\Delta x$ and $\Delta y$, which should be compatible with available population data. This translates the double integral into a double summation.

$$P_{\mathrm{c},2\sigma} \approx A_\mathrm{c} \sum_{-N_{2\sigma}}^{+N_{2\sigma}} \sum_{-M_{2\sigma}}^{+M_{2\sigma}} P_\mathrm{i}(x_n, y_m) \cdot \rho(x_n, y_m) \tag{9}$$

Here, $x_n = n \cdot \Delta x$ and $y_m = m \cdot \Delta y$ mark the bin centers, with $-N_{2\sigma} \leq n \leq +N_{2\sigma}$ and $-M_{2\sigma} \leq m \leq +M_{2\sigma}$, and $P_\mathrm{i}(x_n, y_m) = p_\mathrm{i}(x_n, y_m) \cdot \Delta y\, \Delta x$ is the bin-wise impact probability. A summation over the rectangular area given by Eq.9 covers 46.6% of the 2D impact probability for a $1\sigma$ distribution, and 91.1% for a $2\sigma$ distribution. The latter one is considered in ESA predictions by assuming a $\pm 20\%$ uncertainty on the remaining orbit lifetime, with a corresponding uncertainty in the re-entry footprint extension. The validity of this adopted uncertainty was verified through 15 IADC re-entry prediction campaigns.

## 4. THE RE-ENTRY OF ROSAT

The German ROSAT (Röntgen Satellit/X-ray satellite, Fig. 4) shall serve as an example of an ESA re-entry prediction campaign. ROSAT was launched on June 1, 1990, with a Delta-2 launcher from Kennedy Space Center. It was registered under COSPAR ID 1990-049A and US Catalog Number 20638. The spacecraft of dry mass 2,400 kg and dimensions 2.2 m × 4.7 m × 8.9 m was deployed in an initial orbit of altitude 565 km × 584 km and inclination $53.0^\circ$.

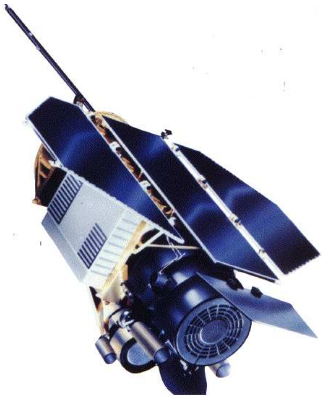

*Figure 4. The German ROSAT (Röntgensatellit).*

After a highly successful mission in which 125,000 new X-ray sources were detected and X-ray background radiation of quasars and galaxies was analysed, the spacecraft was switched off on February 12, 1999, after exceeding it expected mission lifetime by almost a factor 2. The spacecraft that was designed with no orbit maneuvering capability subsequently started its natural orbit decay during the ascending phase of solar cycle 23.

By October 10, 2011, ROSAT had decendent to an altitude of 240 km × 256 km at $52.95^\circ$ inclination. On request of DLR, at this point in time an IADC re-entry

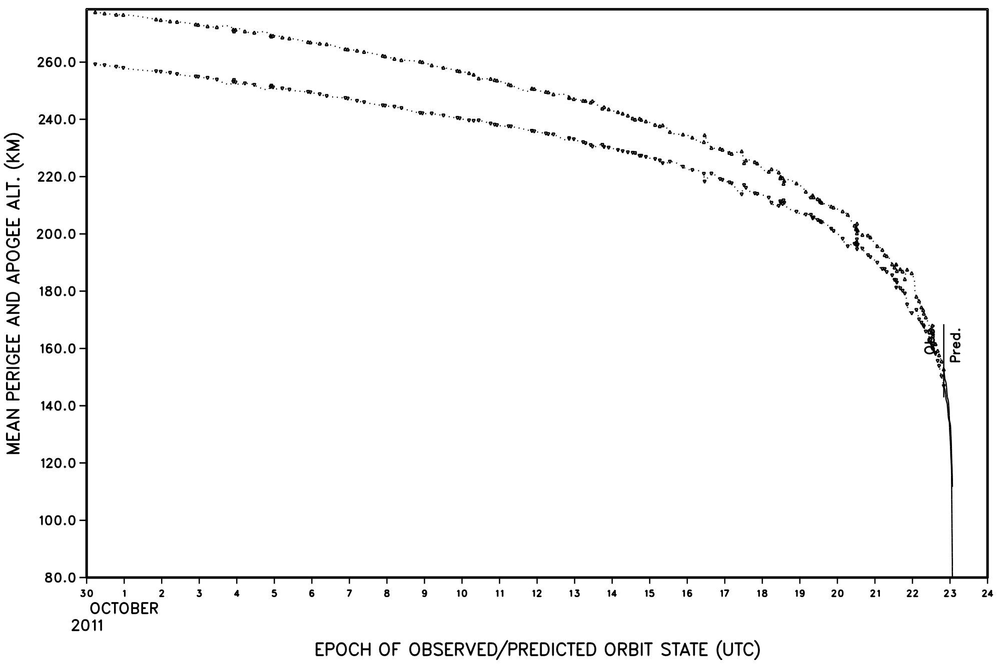

*Figure 1. Apogee and perigee altitude decay history during the final re-entry phase of ROSAT, as a function of the orbit state epoch, in terms of mean (singly averaged) elements.*

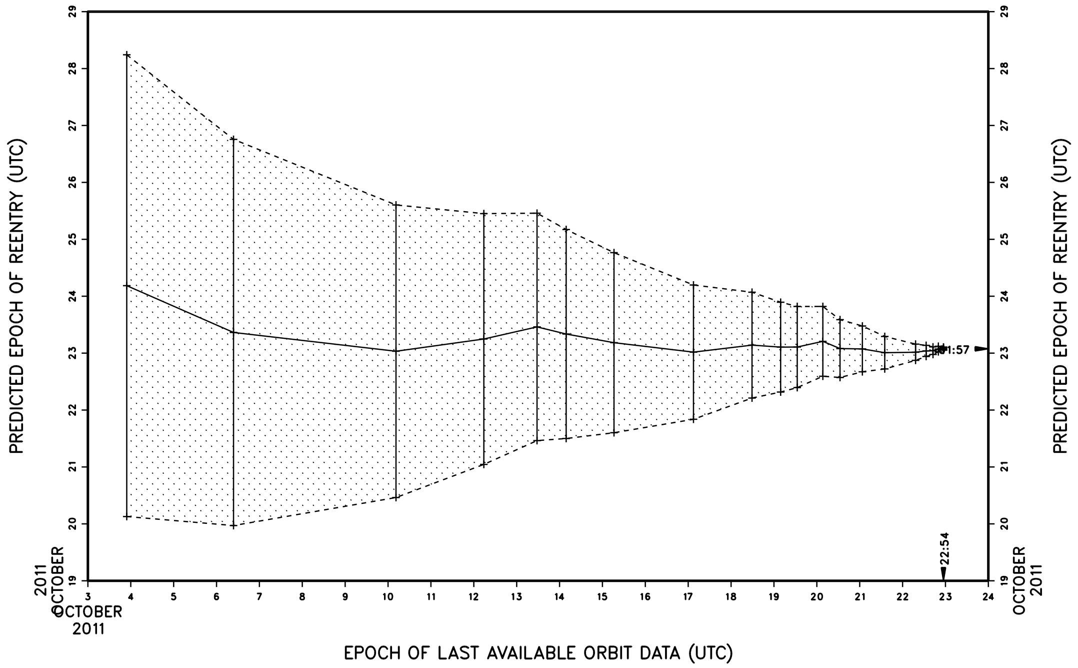

*Figure 2. ESA predictions of the ROSAT re-entry time (solid line) and its associated uncertainty bounds (dashed lines) during the final decay phase, as a function of the epoch of the last available orbit state. The adopted re-entry epoch was* $t_{\mathrm{COIW}}$ *= 2011/10/23 01:57 UTC, corresponding to the pass of a 10 km reference altitude.*

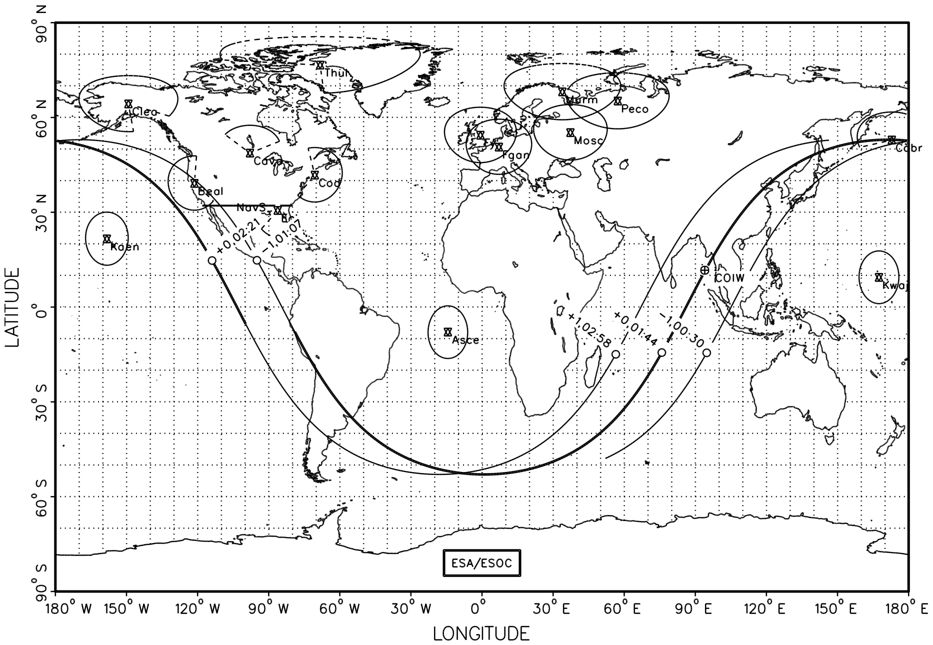

*Figure 3. Ground track of ROSAT for its final re-entry phase. The solid track marks ESA's re-entry time window for the last prediction at* $t_{\mathrm{COIW}} - 3$ *h, with an uncertainty of* $\pm 37$ *min. The "*$\bigoplus$*" symbol marks the adopted re-entry location for a 10 km reference altitude, corresponding to a re-entry epoch of* $t_{\mathrm{COIW}} =$ *2011/10/23 01:57 UTC.*

prediction campaign was initiated for the decaying satellite.

The start of such a campaign implies the official opening of the IADC Re-Entry Events Database (REDB) that is hosted and operated by ESA's Space Debris Office in Darmstadt/Germany. Each of the 12 IADC Members can opt to participate in such a campaign. In that case, they receive a campaign-specific access code that allows them to contribute own data and retrieve data from other participants on orbit determinations and re-entry forecasts. During approximately 13 days between the ROSAT campaign opening and the confirmed re-entry 224 orbit states were uploaded (215 in Two-Line Element format and 9 as osculating state vectors). In the same time frame, 157 re-entry predictions were entered, with 58 thereof during the last 48 hours.

Fig. 1 shows the observed evolution of the mean apogee- and perigee altitude of ROSAT during the last 24 days of its orbital lifetime. Fig. 2 indicates how ESA's predictions of the re-entry time evolved in the same time span, with the most probable entry time $t_{COIW}$ (COIW = "center of impact window") shown as a solid line, as a function of the time of the last available orbit state. The re-entry time window is indicated by symmetric, dashed lines that mark an uncertainty of ±20% of the remaining orbit lifetime. At the start of the campaign (at $t_{\mathrm{COIW}} - 13$ days) the re-entry time window was $\pm 2.6$ days wide. If the assumed uncertainty (i.e. $\pm 20\%$) was properly chosen, then a horizontal line drawn towards the left from any of the data points $t_{\mathrm{COIW}}(t)$ should not touch the bounding curves of the time window. This was the case for ROSAT.

The last orbit state that was available for an ESA re-entry forecast of ROSAT was from 2011/10/22 22:54:52 UTC. It led to a predicted re-entry time at 2011/10/23 02:05:52 UTC, for a reference altitude of 10 km, with a remaining uncertainty of $\pm 37$ minutes, that translates into about $\pm 0.4$ orbits, as indicated by the solid ground track in Fig. 3.

The US Joint Space Operations Center (JSpOC) reported that ROSAT passed through a so-called "80 km altitude interface" at 2011/10/23 01:50 UTC and 90.0°E/7.0°N. The corresponding pass of the 10 km reference altitude occurs about 7 minutes later (at 01:57 UTC) over the gulf of Bengal, not far from the coast line. ESA's final forecast overshot this observation-based reference by almost 8 minutes, but it was well within the expected uncertainty time window of $\pm 37$ minutes.

Under a special agreement ESA also provided to DLR data on land impact probability and on casualty probability during the final phase of the ROSAT re-entry. These assessments were based on Eq.9 for the evolving $2\sigma$ extension of the ground impact swath with progressing time, applying a casualty cross-section of $A_c = 32\mathrm{m}^2$. This figure, provided by DLR, was derived by means of the sophisticated SCARAB tool (spacecraft atmospheric re-entry and aerothermal break-up) by simulating the ROSAT re-entry with a realistic geometry, mass and material model of the spacecraft, by exposing it to mechanical and heat loads of a re-entry, and by following resulting break-up fragments to demise or ground impact.

## 5. ESA RE-ENTRY PREDICTION FEATURES

ESA's Space Debris Office has a history of more than 30 years of re-entry predictions and risk assessments. During this time span a comprehensive suite of software tools has been developed in house or through industrial contacts. Today, the following facets to a complete assessment picture of a re-entry event are available:

- CPU-time efficient long-term, semi-analytical orbit prediction
- robust and accurate short-term numerical re-entry trajectory prediction
- calibration of spacecraft drag parameters through retro-fits of observed histories of the mean semimajor axis
- use of comprehensive perturbation models for the orbital and atmospheric flight regime, with customized atmosphere models, and supporting predictions of solar and geomagnetic activities
- off-line analysis tools to determine the effective cross-section, aerodynamic coefficients, attitude dynamics, break-up (under mechanical and thermal loads), demise, or ground impact (with event-specific casualty cross-section)
- real-time analysis tools to assess the re-entry time, its uncertainty, and the endangered ground swath, with related land impact and population casualty probabilities
- detailed reporting at well-defined frequencies, with standardized formats during an entire re-entry campaign in a 24/7 fashion

Upon request, these services are available to ESA Member States and (via ESA/DG-C) to entities outside ESA.

Best results are achieved during IADC re-entry prediction campaigns, mainly because of the abundance and different sources of orbit determination data, which in the case of ROSAT originated from NASA, ROSCOSMOS, DLR, CNES and ESA, with a total of 341 orbit states of which 49 were made available during the last 48 h of the campaign. Moreover, IADC campaigns can use "hard data" from surveillance systems as benchmarks for validating re-entry prediction times and positions.

## 6. CONCLUSIONS AND OUTLOOK

Since 1982 ESA has developed capabilities and implemented tools to perform re-entry forecasts and to assess related risks for the population in the endangered ground swaths. Related services are offered by the Space Debris Office in a 24/7 fashion to ESA Member States.

Based on 15 well-monitored IADC re-entry prediction campaigns since 1998, with well-established, observed re-entry times and locations, ESA's predictions were found to be within $\pm 6\%$ of the remaining orbital lifetime for about 50% of all cases, within $\pm 10\%$ for about 75%, and outside $\pm 20\%$ for about 5% of all forecasts. The latter figure supports ESA's a priori assumption that a re-entry time window of $\pm 20\%$ is a good representation of agregate error sources, leading to a $\pm 2\sigma = 94.4\%$ confidence interval.

If possible, all entry objects of masses exceeding 1,000 kg should be analysed for their effective casualty cross-section prior to the start of an entry campaign. On the average, objects with $m \approx 1,000$ kg will exceed a threshold value of $A_c \approx 6\mathrm{m}^2$ (corresponding to an internationally accepted casualty probability treshold of $P_{\mathrm{c,max}} = 1$ in 10,000 per event) for 70% to almost 100% of all cases (depending on the orbit inclination). These figures reduce to 40% to 80% for a 400 kg object, and to 0% to 50% for a 200 kg object.

ESA's Space Debris Office is presently developing tools to generate more detailed re-entry prediction output data that can be presented both in tabular and graphical formats, with extended, high-resolution information content. Such output formats will further facilitate the interpretation of re-entry risks by national civil protection entities.

## REFERENCES

1. Klinkrad H., (1985). Long-Term Analytical Orbit Decay and Re-Entry Prediction, in Proceedings of a International Workshop on Re-Entries of Space Debris, Darmstadt, 24-25 Sept. 1985, *ESA SP-246*, p.39–48
2. Klinkrad H., (1991). Salyut-7/Cosmos-1686 Re-Entry Prediction Activities at ESOC, in Proceedings of an international Workshop on the Salyut-7/Cosmos-1686 Re-Entry, Darmstadt, 9 April 1991, *ESA SP-345*, p.17–34
3. Klinkrad H., Flury W., Hernández C., Landgraf M., Jehn R., Christ U., Sintoni F., (2001). ESOC Activities during the Mir De-Orbit, in Proceedings of an international Workshop on the Mir De-Orbit, Darmstadt, 14 May 2001, *ESA SP-498*, p.57–66
4. Klinkrad H., (2006). *Space Debris – Models and Risk Analysis*, Springer-Praxis, Berlin/Heidelberg/New York
5. Rex D., (1980). Der Wiedereintritt großer Satelliten in die Erdatmosphäre – Risiko und Vorausberechnung (in German), *Zeitschrift für Flugwissenschaften und Weltraumforschung*, **4**(6), p.354–365